

# **Combining Schwarz-Christoffel Mappings and Biot-Savart Law to Calculate the High-Frequency Current Distribution Inside a Single Slot**

Torben Fricke<sup>1</sup>, Phil Leon Pickert<sup>1</sup>, Babette Schwarz<sup>2</sup>, Bernd Ponick<sup>1</sup>

LEIBNIZ UNIVERSITY HANNOVER<sup>1</sup>, VOITH HYDRO HOLDING GMBH & CO. KG<sup>2</sup>

Institute for Drive Systems and Power Electronics<sup>1</sup>

Hannover, Germany<sup>1</sup> and Heidenheim an der Brenz, Germany<sup>2</sup>

Email: torben.fricke@ial.uni-hannover.de

URL: <https://ial.uni-hannover.de><sup>1</sup> and <https://voith.com><sup>2</sup>

## **Keywords**

«Converter machine interactions», «Electrical machine», «Adjustable speed drive», «Software»

## **Abstract**

A novel calculation approach for the current and field distribution inside conductors in a slot at high frequencies based on a combination of a Schwarz-Christoffel Mapping and Biot-Savart Law is presented. The stator and rotor laminations are modeled using a surface impedance boundary condition and the results are validated against 2D FEA. The proposed method is overall less capable and mature than widely available 2D FEA software but has some appeal in niche applications, where licensing issues with FEA software are of concern or a high degree of integration into a broader tool chain is desirable.

## **Introduction**

The proliferation of wide-bandgap semiconductors makes higher efficiencies and smaller form factors possible in power electronics [1]. These technological advances pose challenges in the design of electrical machines, as the increased switching speed exaggerates problems related to high frequency (HF) leakage currents [2]. Designing electrical machines that are resilient to adverse effects from HF voltage components requires advanced calculation approaches to predict high frequency leakage currents. One important component of such a calculation approach is an HF model of the stator winding. The inductances, resistances and capacitances of the stator winding HF model are commonly calculated using 2D FEA [3]. In this paper, an alternative calculation approach based on a combination of a Schwarz-Christoffel (SC) mapping and Biot-Savart (BS) law is presented and evaluated. The idea of combining Biot-Savart law with a conformal mapping dates back to 1979, when Reppe [4] used a numerically solved SC mapping in combination with BS law to calculate the air-gap field in a salient-pole synchronous machine. This combination of methods has since been used in geophysics [5], the current distribution calculation in PCB traces [6], superconductor research [7] and, of course, field problems in electrical machines [8]. In this paper, the idea of combining an SC mapping with BS law will be extended to new HF field problems by introducing a surface impedance boundary condition.

## **Method**

The algorithm used to calculate the current distribution inside an arbitrary number of conductors in a slot can be summarized by the following steps, which will be explored in the subsequent subsections.

1. Solve the Schwarz-Christoffel mapping for the desired geometry.
2. Discretize each conductor into a number of partial conductors with a constant current distribution.
3. Generate surface conductors that represent a surface impedance boundary condition (SIBC).

4. Generate the surface conductor inductance matrix and use it to calculate the SIBC-aware vector potential.
5. Calculate the partial conductor inductance matrix.
6. Solve the partial conductor inductance matrix for the current distribution, taking into account the voltage induced by other distributed conductors. Repeat this step until the current distribution is constant.

### Schwarz-Christoffel Mapping

A conformal mapping is a technique which maps one bound area (or domain) to another while preserving angles locally [9], as seen in Fig. 1. This allows us to solve certain kinds of field problems in one domain and transform the solution to another domain, which is usually more complex. The Schwarz-Christoffel (SC) mapping is one kind of conformal mapping, which maps from an infinite half plane (canonical domain) to an arbitrary polygon (physical domain), as shown in Fig. 4. For simple geometries, this mapping can be calculated analytically. A collection of analytically solved SC mappings is provided by Gibbs [10]. More complex geometries have to be approached numerically, as pioneered by Reppe [4] and later expanded upon by Driscoll, who open sourced his implementation [11]. Further explorations into numerical SC mappings unfortunately cannot be provided in this paper due to space constraints. However, Driscoll's book [9] is a great resource on this matter.

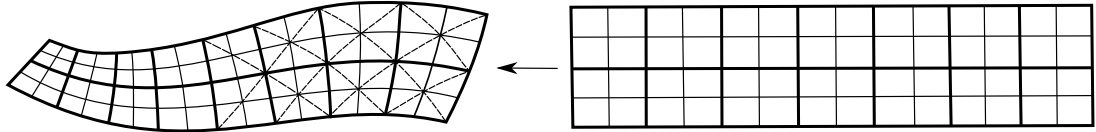
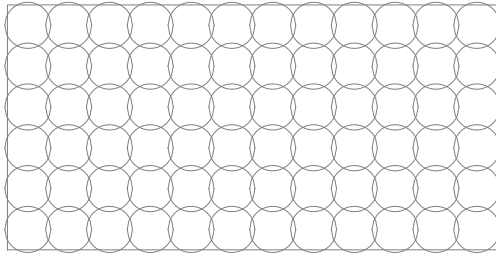
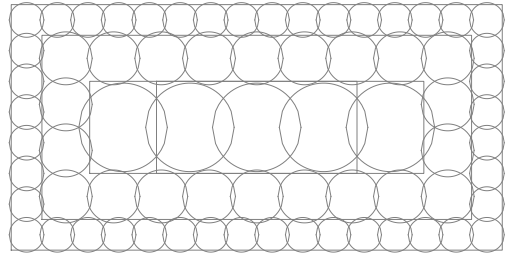


Fig. 1: Example of a conformal mapping. Note how the size and shape of the squares changes, but the angles remain unchanged.

### Discretization



(a) Uniform mesh containing 72 partial conductors



(b) Skin mesh containing 71 partial conductors

Fig. 2: Two ways to discretize a rectangular distributed conductor into circular partial conductors.

Any distributed conductor – be it a hairpin, round wire or Roebel bar subconductor – has to first be discretized into multiple circular partial conductors with a constant current distribution. Fig. 2 shows two ways in which a distributed conductor can be discretized. The total area of all partial conductors equals the area of the distributed conductor. The field of a partial conductor can now be calculated using the geometric vector potential

$$GVP = \frac{1}{4\pi} \cdot \begin{cases} \left( \frac{r^2}{R^2} + \ln(R^2) - 1 \right) & \text{inside the conductor } (r \leq R) \\ \ln(r^2) & \text{outside of the conductor } (r > R), \end{cases} \quad (1)$$

which has been defined such that the vector potential outside a partial conductor is independent of its radius (this property will become important later on). The geometric vector potential GVP (shown in Fig. 3) can easily be turned into the vector potential

$$\underline{A} = GVP \cdot \underline{I} \cdot \mu_r \mu_0, \quad (2)$$

where the current  $\underline{I}$  is defined as an RMS phasor.

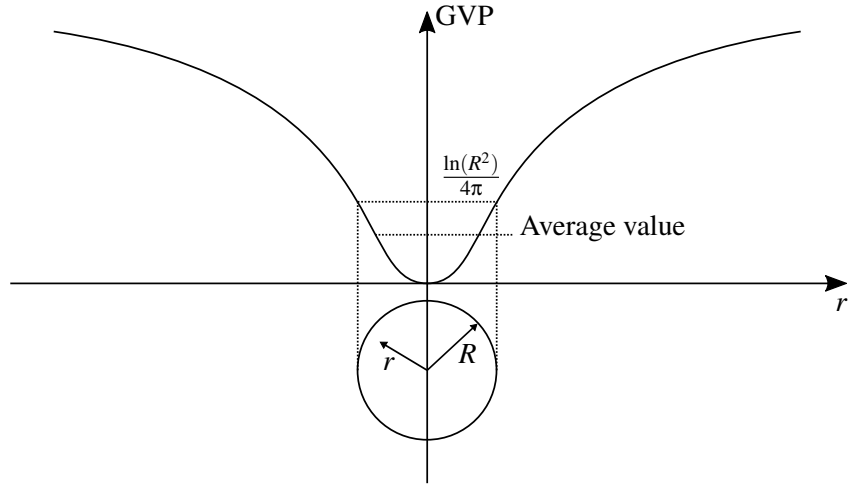


Fig. 3: Geometric vector potential (GVP) of a circular conductor carrying a constant current

The vector potential is calculated in the canonical domain using the method of image currents. When using BS law in combination with a conformal mapping, the image current

$$I' = \begin{cases} I & \mu \rightarrow \infty \text{ field lines are normal to the surface} \\ -I & \mu = 0 \text{ field lines are tangential to the surface} \end{cases} \quad (3)$$

can only take one of two values. Mapping a field solution obtained using any other image current produces an incorrect result. Fig. 4 shows the field produced by a line conductor arbitrarily placed in an arbitrary physical mapping. The field solution has been calculated in the canonical domain and transformed into the physical domain. All Biot-Savart calculations, even those of the surface currents introduced in the next section, are performed in the canonical domain, assuming  $\mu \rightarrow \infty$ , and mapped into the physical domain.

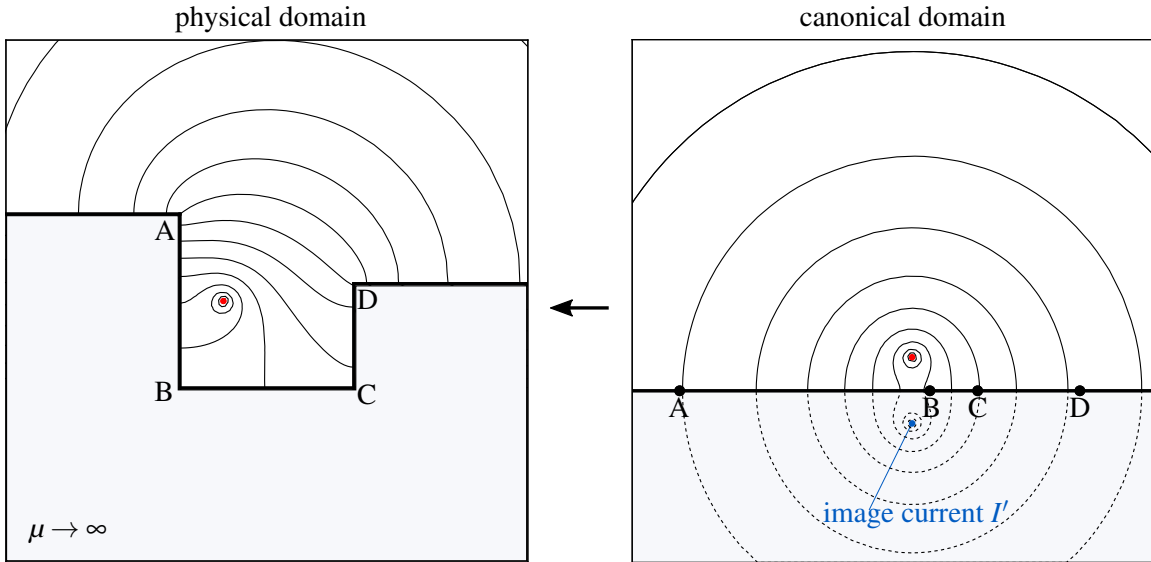


Fig. 4: Method of image currents in an arbitrary SC mapping

## Surface Conductors

Next, the surface impedance boundary condition (SIBC) can be applied. In this work, the simplest surface impedance boundary condition, often referred to as the skin effect [12], is used. Using this

surface impedance boundary condition requires some assumptions. First, the stator and rotor material has to be assumed to have a constant permeability  $\mu_r$  and conductivity  $\sigma$ . All geometric features at the boundary must be small compared to the skin depth

$$\delta = \frac{1}{\sqrt{\pi f \sigma \mu_r \mu_0}}. \quad (4)$$

Assuming a typical conductivity for M330-35A electrical steel of  $\sigma = 2.2 \text{ MS/m}$  [13] and a permeability of  $\mu_r = 2000$ , this requires the frequency to be higher than about 5000 Hz for the skin depth  $\delta(f = 5000 \text{ Hz}) = 0.11 \text{ mm}$  to become sufficiently small compared to a common lamination thickness of 0.35 mm. In cases where the teeth are saturated from the fundamental harmonic, the frequency needs to be higher for this assumption to remain valid. The surface impedance can be written as

$$\underline{Z}_s'' = \frac{1+j}{\sigma \delta} \quad (5)$$

and has the unit  $[\underline{Z}_s''] = \Omega/\text{m}^2$ .

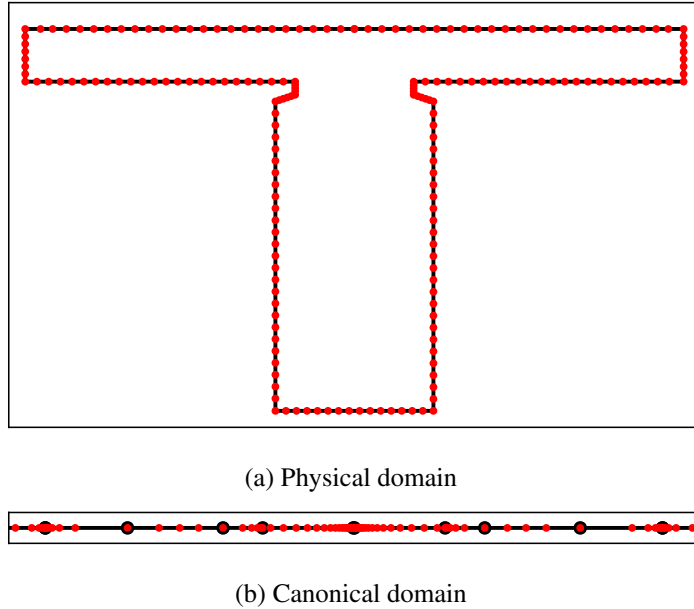


Fig. 5: Locations of surface conductors in both domains of the SC mapping.

In order to discretize the SIBC for use in the proposed calculation approach, surface conductors are applied along the edges of the SC mapping polygon as shown in Fig. 5. The surface conductors are spaced uniformly along each edge, with shorter edges having a higher conductor density. Now the surface impedance per unit depth (all impedances and voltages are per unit depth) can be calculated as

$$\underline{Z}_k' = \underline{Z}_s'' \cdot \frac{d_{k-1} + d_k}{2}, \quad (6)$$

where  $d_k$  and  $d_{k-1}$  are the distances to the neighboring surface conductors, measured in the physical domain as shown in Fig. 6.

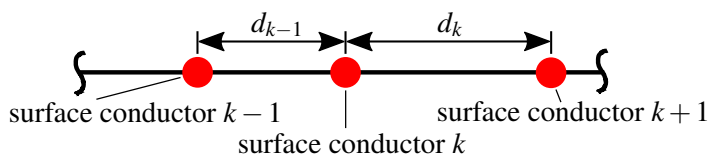


Fig. 6: Distances to neighboring surface conductors measured in the physical domain.

## SIBC-aware Vector Potential

Now we can assemble the *surface impedance matrix* that links all surface conductors to each other. The surface impedance matrix need only be created once and can be written as

$$\underline{\underline{Z}}'_{\text{surf}} = \begin{pmatrix} \underline{\underline{Z}}'_k & \underline{\underline{Z}}'_{k,k+1} & \underline{\underline{Z}}'_{k,k+2} & \cdots \\ \underline{\underline{Z}}'_{k,k+1} & \underline{\underline{Z}}'_{k+1} & \underline{\underline{Z}}'_{k+1,k+2} & \cdots \\ \underline{\underline{Z}}'_{k,k+2} & \underline{\underline{Z}}'_{k+1,k+2} & \underline{\underline{Z}}'_{k+2} & \cdots \\ \vdots & \vdots & \vdots & \ddots \end{pmatrix}, \quad (7)$$

where each impedance is, as always, defined per unit depth.

The mutual impedance between two arbitrary conductors  $a$  and  $b$

$$\underline{\underline{Z}}'_{a,b} = j\omega (A_{a,\infty} - A_{a,b}) / I_a \quad (8)$$

can be calculated from the vector potential of conductor  $a$  at infinity, carrying a current  $I_a$ ,  $A_{a,\infty} = 0$  and the vector potential of the conductor  $a$  at the other conductor  $A_{a,b}$ . The vector potential at infinity equals  $A_{p,\infty} = 0$  because we assume the current loop of the partial conductor to close at infinity. Therefore, the sum of the vector potentials of the partial conductor and the returning conductor (at infinity) equals zero. This equation is used for every non-diagonal element of the matrix. The diagonal elements of the matrix represent the self-inductance of each surface conductor and are calculated using equation (6).

It is worth inverting the surface impedance matrix  $\underline{\underline{Z}}'_{\text{surf}}$  as it is used repeatedly. Afterwards, the surface currents can be calculated as

$$\underline{\underline{I}}'_{\text{surf}} = \underline{\underline{U}}'_p \cdot \underline{\underline{Z}}'^{-1}_{\text{surf}}. \quad (9)$$

The voltage per length, induced by a partial conductor with the index  $p$ ,

$$\underline{\underline{U}}'_p = I_p \cdot \begin{pmatrix} \underline{\underline{Z}}'_{p,k} \\ \underline{\underline{Z}}'_{p,k+1} \\ \underline{\underline{Z}}'_{p,k+2} \\ \vdots \end{pmatrix} \quad (10)$$

is calculated from its current  $\hat{I}_p$  and the mutual impedance between the partial conductor and each surface conductor, which in turn can be calculated from equation (8).

Now we can introduce the SIBC-aware vector potential

$$\underline{\underline{A}}^* = \underline{\underline{A}}_p + \sum_k \underline{\underline{A}}_{\text{surf},k}, \quad (11)$$

which contains the contribution of a partial conductor itself  $\underline{\underline{A}}_p$  and of the surface currents it causes  $\underline{\underline{A}}_{\text{surf},k} = A(\underline{\underline{I}}_{\text{surf},k})$ . The *SIBC-aware vector potential* allows us to perform Biot-Savart calculations that take the surface impedance boundary condition into account, while abstracting the surface impedance matrix away.

## Partial Conductor Inductance Matrix

Next, the *partial conductor inductance matrix* that describes how the partial conductors of one distributed conductor are linked to each other needs to be generated. This matrix has to be created for each

distributed conductor and can be written as

$$\underline{\mathbf{Z}}'_{\text{part}} = \begin{pmatrix} \underline{\mathbf{Z}}_p' & \underline{\mathbf{Z}}'_{p,p+1} & \underline{\mathbf{Z}}'_{p,p+2} & \dots \\ \underline{\mathbf{Z}}'_{p,p+1} & \underline{\mathbf{Z}}_{p+1}' & \underline{\mathbf{Z}}'_{p+1,p+2} & \dots \\ \underline{\mathbf{Z}}'_{p,p+2} & \underline{\mathbf{Z}}'_{p+1,p+2} & \underline{\mathbf{Z}}_{p+2}' & \dots \\ \vdots & \vdots & \vdots & \ddots \end{pmatrix}, \quad (12)$$

with the nomenclature shown in Fig. 7.

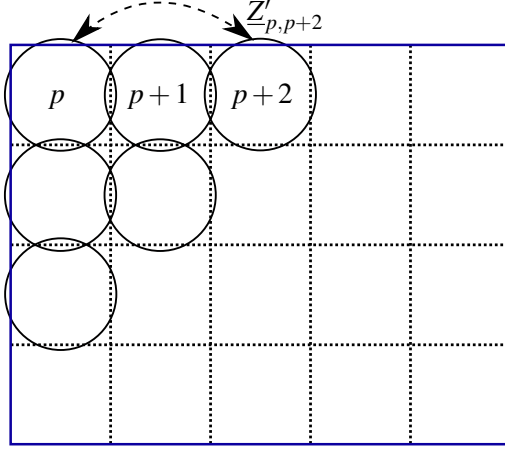


Fig. 7: Nomenclature for the partial conductor inductance matrix. The blue rectangle represents the outline of a distributed conductor.

The non-diagonal elements are obtained similarly to equation (8), only now using the SIBC-aware vector potential:

$$\underline{\mathbf{Z}}'_{a,b} = j\omega (\underline{\mathbf{A}}_{a,\infty}^* - \underline{\mathbf{A}}_{a,b}^*) / I_a \quad (13)$$

The diagonal elements contain the self-impedance of each partial conductor

$$\underline{\mathbf{Z}}'_p = \frac{1}{\sigma \cdot \pi R^2} + j\omega (\underline{\mathbf{A}}_{p,\infty}^* - \underline{\mathbf{A}}_p^*) / I_p, \quad (14)$$

where the first term accounts for the partial conductor's resistance, with  $\sigma$  being the conductivity of the corresponding distributed conductor. The second term represents the self-inductance of the partial conductor, where  $\underline{\mathbf{A}}_{p,\infty}^* = 0$  is the vector potential at infinity and  $\underline{\mathbf{A}}_p^*$  is the vector potential caused by the partial conductor in question, at its center.

## Current Distribution

Finally, we can calculate the actual current distribution inside a distributed conductor. The current carried by the distributed conductor is set as an input value, while its voltage is a result of the current distribution. Fig. 8 gives an overview of how the current distribution is calculated.

First, the terminal voltage along the distributed conductor is set to an initial, virtually infinite value  $U'_{\text{terminal}} = 10^{10} \text{ V/m}$ .

Next, the voltage induced by other distributed conductors is determined by calculating the mutual inductance between each external partial conductor and each partial conductor of the distributed conductor in question using equation (13), as shown in Fig. 9. This requires a large number of calculations to be performed. If we assume  $n_{\text{distrib}} = 6$  distributed conductors made up of  $n_{\text{part}} = 70$  partial con-

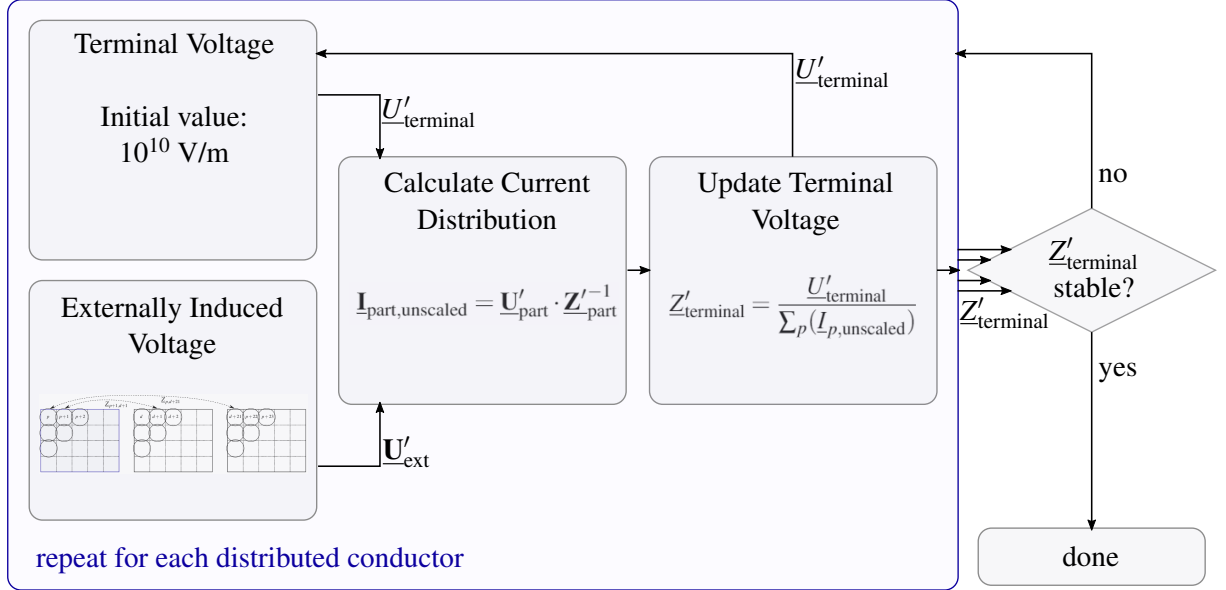


Fig. 8: Flowchart describing how the current distribution is calculated.

ductors each, this involves a total of  $n_{\text{part}} \cdot n_{\text{part}} \cdot (n_{\text{distrib}} - 1) = 24500$  impedance calculations to calculate the externally induced voltage of one distributed conductor. If external distributed conductors are approximated using one effective conductor each, the number of calculations can be reduced to  $n_{\text{part}} \cdot 1 \cdot (n_{\text{distrib}} - 1) \cdot n_{\text{distrib}} = 350$ . This approximation will be used in the validation section, as it provides a worthwhile trade-off between accuracy and calculation time. The voltage induced by other distributed conductors can be written as

$$\mathbf{U}'_{\text{ext}} = \begin{pmatrix} Z'_{p,d} & Z'_{p,d+1} & Z'_{p,d+2} & Z'_{p,d+3} & \dots \\ Z'_{p+1,d} & Z'_{p+1,d+1} & Z'_{p+1,d+2} & Z'_{p+1,d+3} & \dots \\ Z'_{p+2,d} & Z'_{p+2,d+1} & Z'_{p+2,d+2} & Z'_{p+2,d+3} & \dots \\ \vdots & \vdots & \vdots & \vdots & \ddots \end{pmatrix} \cdot \begin{pmatrix} I_d \\ I_{d+1} \\ I_{d+2} \\ I_{d+3} \\ \vdots \end{pmatrix}, \quad (15)$$

where  $I_d, I_{d+1}, \dots$  refer to the partial conductor currents in the external distributed conductors (or the effective conductor which it has been approximated by), while the indices  $p, p+1, \dots$  refer to the partial conductors of the distributed conductor in question, as shown in Fig. 9.

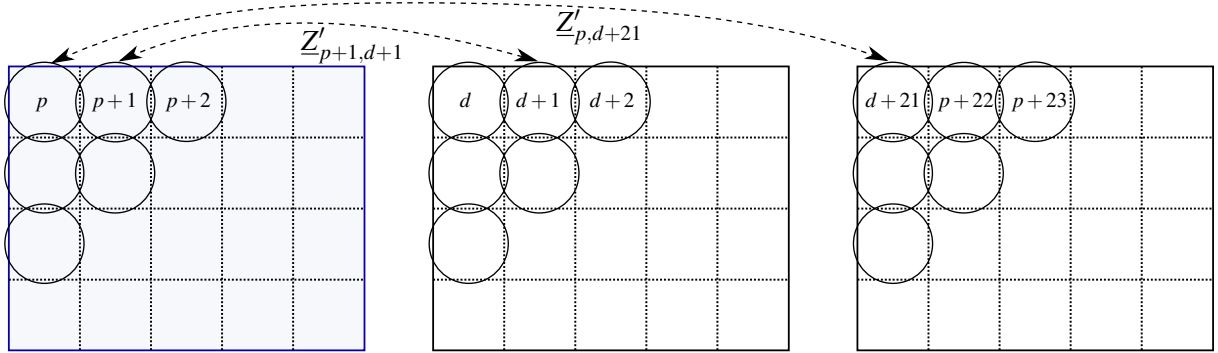


Fig. 9: Nomenclature indicating how the mutual inductances between the partial conductors of the distributed conductor in question and those of external distributed conductors relate.

The partial conductor voltage vector

$$\underline{\mathbf{U}}'_{\text{part}} = U'_{\text{terminal}} + (\underline{\mathbf{U}}'_{\text{ext}} - \text{mean}(\underline{\mathbf{U}}'_{\text{ext}})) \quad (16)$$

is a result of the terminal voltage and the voltage induced by external distributed conductors. Now, the current distribution can be calculated as

$$\underline{\mathbf{I}}_{\text{part,unscaled}} = \underline{\mathbf{U}}'_{\text{part}} \cdot \underline{\mathbf{Z}}'^{-1}_{\text{part}}, \quad (17)$$

where the partial conductor inductance matrix  $\underline{\mathbf{Z}}'_{\text{part}}$  has been inverted to avoid solving a system of equations in each iteration. Next, the current distribution is scaled

$$\underline{\mathbf{I}}_{\text{part}} = \underline{\mathbf{I}}_{\text{part,unscaled}} \cdot \frac{I_{\text{terminal}}}{\sum_p (I_{p,\text{unscaled}})} \quad (18)$$

so that the sum of all partial currents equals the terminal current  $I_{\text{terminal}}$ .

Lastly, the apparent terminal impedance

$$\underline{\mathbf{Z}}'_{\text{terminal}} = \frac{U'_{\text{terminal}}}{\sum_p (I_{p,\text{unscaled}})} \quad (19)$$

is calculated, and the terminal voltage is updated for the next iteration

$$U'_{\text{terminal}} = \underline{\mathbf{Z}}'_{\text{terminal}} \cdot I_{\text{terminal}}. \quad (20)$$

These steps are performed for each distributed conductor. Afterwards, the whole process is repeated until the change in terminal impedance  $\underline{\mathbf{Z}}'_{\text{terminal}}$  between two iterations is below a threshold value in every distributed conductor.

## Validation

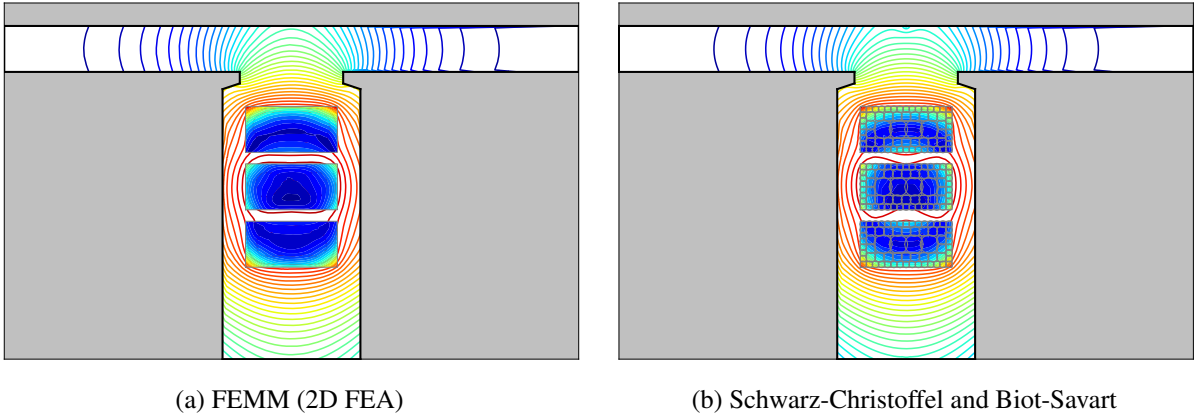
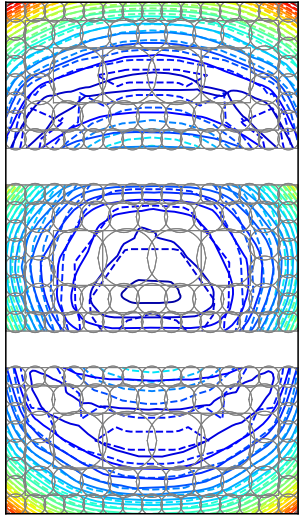
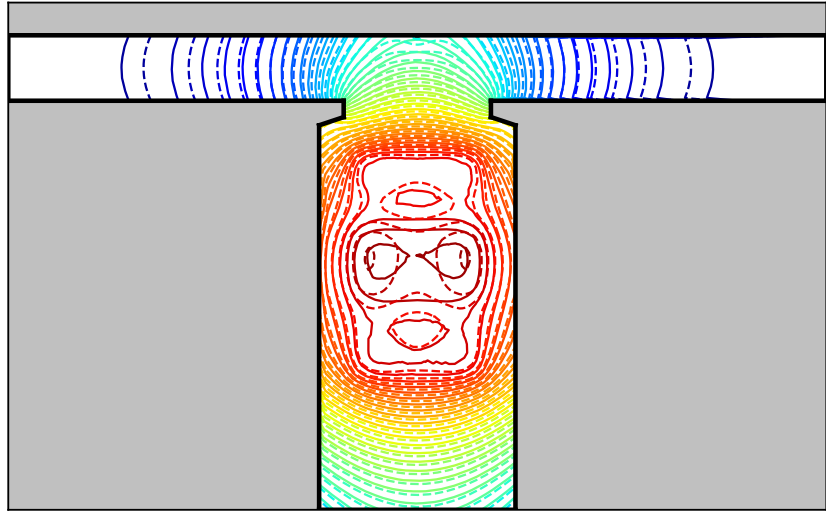


Fig. 10: Flux lines and current distribution in a slot.

The proposed calculation approach was validated by comparing it to 2D FEA simulations using the open-source FEMM software [14]. The geometry, material properties, and boundary conditions were kept the same in both calculations. In FEMM, the corresponding boundary condition is called *Small Skin Depth* and was assigned to every edge enclosing the simulation domain. Fig. 10 shows the current distribution and the field lines (lines of constant vector potential) for the case where every conductor carries the same current. For the Schwarz-Christoffel and Biot-Savart calculation, external distributed conductors were approximated using an effective conductor, as described earlier.



(a) Current density



(b) Vector potential

Fig. 11: Comparison between the 2D FEA simulation (solid lines) and the Schwarz-Christoffel and Biot-Savart based approach (dotted lines).

Plotting the current distribution and the field lines from these calculations together, as shown in Fig. 11 allows us to assess the differences between the calculations more clearly. While there are easily noticeable differences in both the current distribution and field lines, they are overall acceptable given the likely much higher error, compared to reality, due to the simplifications made to allow for the SIBC and only considering one slot. Fig. 12 shows a more complex example of what the proposed method is capable of, with twelve conductors within one slot being modeled.

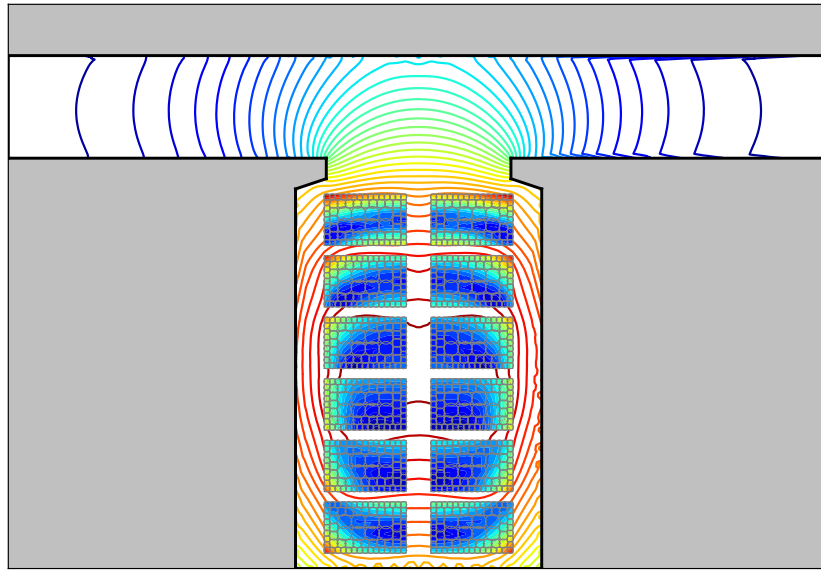


Fig. 12: A more complex example of a current distribution, calculated using the Schwarz-Christoffel and Biot-Savart based approach.

## Conclusion

The proposed Schwarz-Christoffel and Biot-Savart based approach is able to accurately calculate the current distribution of conductors within a single slot. A key difference from 2D FEA is the fact that the field can be calculated wherever it is needed instead of meshing the entire domain.

Using the proposed method currently requires a deep understanding of how Schwarz-Christoffel mappings are solved numerically in order to circumvent numerical challenges such as crowding and inverse mapping convergence issues [9]. Given how mature 2D FEA software has become, it is hard to make the case that a combination of Schwarz-Christoffel mappings and Biot-Savart law should become a general-purpose field and loss calculation tool. However, the proposed method is appealing in niche applications where licensing costs or restrictions of FEA software are an issue or where a high level of integration into a broader toolchain and the possible benefits in calculation time resulting from only having to calculate the field where it is needed, are worth the implementation effort.

## References

- [1] F. D. Giovanni. *Wide Bandgap Semiconductors: to EV and beyond*. Power Electronics News. 2020. URL: <https://www.powerelectronicsnews.com/wide-bandgap-semiconductors-to-ev-and-beyond/> (visited on 11/2021).
- [2] G. Grandi, D. Casadei, and U. Reggiani. “Common- and differential-mode HF current components in AC motors supplied by voltage source inverters”. In: *IEEE Transactions on Power Electronics* 19.1 (2004). Conference Name: IEEE Transactions on Power Electronics, pp. 16–24. DOI: 10.1109/TPEL.2003.820564.
- [3] B. Heidler, K. Brune, and M. Doppelbauer. “High-frequency model and parameter identification of electrical machines using numerical simulations”. In: *2015 IEEE International Electric Machines Drives Conference (IEMDC)*. 2015, pp. 1221–1227. DOI: 10.1109/IEMDC.2015.7409217.
- [4] K. Reppe. *Berechnung von Magnetfeldern mit Hilfe der konformen Abbildung durch numerische Integration der Abbildungsfunktion von Schwarz-Christoffel*. Vol. 8. Siemens Forschungs- und Entwicklungsberichte. Heidelberg, Germany: Springer., 1979.
- [5] P. Janhunen and A. Viljanen. “Application of conformal mapping to 2-D conductivity structures with non-uniform primary sources”. In: *Geophysical Journal International* 105.1 (1991), pp. 185–190. DOI: 10.1111/j.1365-246X.1991.tb03454.x.
- [6] V. V. Amelichev et al. “Conformal transformation method as applied to finding the current density distribution and induced magnetic field in a strip conductor with a rectangular cut”. In: *Computational Mathematics and Mathematical Physics* 54.10 (2014), pp. 1618–1625. DOI: 10.1134/S0965542514100017.
- [7] E. Costamagna, P. Di Barba, and R. Palka. “Field models of high-temperature superconductor devices for magnetic levitation”. In: *Engineering Computations: Int J for Computer-Aided Engineering* 29 (2012). DOI: 10.1108/02644401211246328.
- [8] D. C. J. Krop, E. A. Lomonova, and A. J. A. Vandenput. “Application of Schwarz-Christoffel Mapping to Permanent-Magnet Linear Motor Analysis”. In: *IEEE Transactions on Magnetics* 44.3 (2008). Conference Name: IEEE Transactions on Magnetics, pp. 352–359. DOI: 10.1109/TMAG.2007.914513.
- [9] T. Driscoll and L. Trefethen. *Schwarz-Christoffel Mapping*. Cambridge Monographs on Applied and Computational Mathematics. Cambridge University Press, 2002.
- [10] W. J. Gibbs. *Conformal transformations in electrical engineering*. Chapman & Hall, 1958.
- [11] T. A. Driscoll. “An improved Schwarz-Christoffel Toolbox for Matlab”. In: *Department of Mathematical Sciences, University of Delaware* (2003).
- [12] S. V. Yuferev and N. Ida. *Surface Impedance Boundary Conditions: A Comprehensive Approach*. CRC Press, 2009.
- [13] *isovac® - Elektroband, Elektroblech, Generatorenbau*. URL: <https://www.voestalpine.com/isovac> (visited on 11/2021).
- [14] D. Meeker. *Finite Element Method Magnetics (FEMM)*. URL: <http://www.femm.info/wiki/HomePage> (visited on 11/2019).